



# Dislocation-mediated strain hardening in tungsten: Thermo-mechanical plasticity theory and experimental validation



Dmitry Terentyev<sup>a,\*</sup>, Xiazi Xiao<sup>b,d</sup>, A. Dubinko<sup>a,c</sup>, A. Bakaeva<sup>a,c</sup>,  
Huiling Duan<sup>b,d,\*\*</sup>

<sup>a</sup> Structural Material Group, Institute of Nuclear Materials Science, SCK CEN, Mol, Belgium

<sup>b</sup> State Key Laboratory for Turbulence and Complex System, Department of Mechanics and Engineering Science, College of Engineering, Peking University, Beijing 100871, PR China

<sup>c</sup> Department of Applied Physics, Ghent University, St. Pietersnieuwstraat 41, 9000 Ghent, Belgium

<sup>d</sup> CAPT, HEDPS and IFSA Collaborative Innovation Center of MoE, Peking University, Beijing 100871, PR China

## ARTICLE INFO

### Article history:

Received 30 April 2015

Received in revised form

21 August 2015

Accepted 25 August 2015

Available online 28 August 2015

### Keywords:

Tungsten

Crystal plasticity

Hardening

Dislocations

### PACS:

62.20.mt

81.40.Np

81.05.Bx

83.10.Rs

## ABSTRACT

A self-consistent thermo-mechanical model to study the strain-hardening behavior of polycrystalline tungsten was developed and validated by a dedicated experimental route. Dislocation–dislocation multiplication and storage, as well dislocation–grain boundary (GB) pinning were the major mechanisms underlying the evolution of plastic deformation, thus providing a link between the strain hardening behavior and material's microstructure. The microstructure of the polycrystalline tungsten samples has been thoroughly investigated by scanning and electron microscopy. The model was applied to compute stress–strain loading curves of commercial tungsten grades, in the as-received and as-annealed states, in the temperature range of 500–1000 °C. Fitting the model to the independent experimental results obtained using a single crystal and as-received polycrystalline tungsten, the model demonstrated its capability to predict the deformation behavior of as-annealed samples in a wide temperature range and applied strain. The relevance of the dislocation-mediated plasticity mechanisms used in the model have been validated using transmission electron microscopy examination of the samples deformed up to different amounts of strain. On the basis of the experimental validation, the limitations of the model are determined and discussed.

© 2015 Elsevier Ltd. All rights reserved.

## 1. Introduction

The response of structural or functional materials to impact, cyclic or shock mechanical or thermal loading conditions is of practical concern for a variety of nowadays applications, including structural crashworthiness, ballistic events, and explosive–structure interactions. Often, materials owing the needed properties are heterogeneous or at least exhibit a complex microstructure, if considered at the micro-scale, for example polycrystalline metals, fiber reinforced composites, metallic laminates (see e.g. [1,2]). Modern computational science dealing with plasticity phenomenon underlines a role played by

\* Corresponding author.

\*\* Corresponding author at: CAPT, HEDPS and IFSA Collaborative Innovation Center of MoE, Peking University, Beijing 100871, PR China.

dislocations and GBs which practically define the trans-granular (i.e. at nano- to micro-scale level) and inter-granular (at micro- to meso-scale level) plastic deformation (see e.g. [3,4]). Hence, desirable mechanical properties of a certain metallic matrix for extreme applications can be achieved by optimizing its microstructure. That is why many efforts are currently put on the exploration of the relationship of microstructure and mechanical response to gain physical understanding implantable in the fast developing computational models (see e.g. [5,6]).

The international program on thermonuclear fusion is one of the examples, where the application of materials in extreme environmental conditions cannot be avoided [7]. Refractory metals, and in particular tungsten (W) is one of the materials that will play an important role in the ITER as well as in DEMO projects [8–10]. It is a promising plasma facing material for both the divertor and the first wall because of its high melting temperature and resistance to sputtering by low-energy ions. An important general drawback for structural applications is a relatively low ductile-to-brittle transition temperature (DBTT) of W around 300–400 °C [11]. This transition appears to be controlled by dislocation mobility and microstructural features limiting their multiplication and storage.

Indeed, Brunner and co-workers have been intensively involved in the study of mechanical properties of pure tungsten (W), including both single- and polycrystals. A series of experimental work have been performed to study the plastic properties of high-purity tungsten single crystals [12–14]. It was indicated that the appearance of the work hardening mode in tungsten single crystals is closely related to the transition temperature being  $(0.1–0.2)T_m$  (the melting point temperature), being dominated by the mobility of screw dislocations [14]. The compression tests, done in pure polycrystalline tungsten in a wide temperature range, revealed a surprisingly moderate ductility [15]. As what concerns the theoretical study of the thermo-mechanical behavior of polycrystalline tungsten, both phenomenological and physically-based models can be found in literature (see e.g. [15,16]), where the major element ensuring plasticity is defined as the thermally activated motion of screw dislocations. However, the mentioned above works put focus on the yield phenomena and therefore considered low temperature interval (below  $0.2T_m$ ), where the strain hardening of polycrystalline tungsten is limited.

For high temperature applications, such as the divertor or armor plates in ITER, the thermal cyclic fatigue and recrystallization are important issues [17]. The deterioration effect of neutron irradiation and plasma uptake comes on the top of the thermal stresses induced by the plasma instabilities.

For a better understanding of the material response to the thermal cyclic load, it is essential to develop physically based approaches integrated into computational codes at the aggregate level to ensure the integrity and optimum performance of fusion reactor components [18]. It is well recognized that fracture as a physical phenomenon is controlled by a series of processes ranging from the atomic scale to the grain-size scale and beyond. At a mesoscopic scale, the determination of the stress/strain fields around a crack tip is of primary importance and finite element (FE) analysis is widely used for the assessment of the mechanical response to external load [4,16]. The inherent feature of any FE computation is the so-called constitutive laws, i.e., the stress–strain relationship of a representative volume element.

In our previous work, we have studied the strain-hardening behavior of commercial tungsten grades in temperature range 500–2000 °C [19], in the frame of a phenomenological model describing the evolution of flow stress as a function of dislocation density [20]. The strain-hardening behavior was sub-divided onto three types depending on test temperature: (i) below 1000 °C, the main source of strain-hardening was the dislocation–interface interaction (low angle GBs in as-received due to forging or hammering and random GBs in as-annealed materials); (ii) at 1000–1500 °C, the pinning of dislocations was assigned to be controlled by random GBs mainly; and (iii) at 1500 °C and above intensive in-situ creep was observed. However, that oversimplified model, based on the two-parameter Kocks and Mecking approach for dislocation density evolution, assumed that the defect density and spacing obstructing dislocation motion remains constant in the course of plastic deformation as well as the model treated the material as medium without any distinction between grains and subgrains. The latter simplification might be an important limiting factor when it comes to channel deformation or grain-boundary slip. Recently, a role played by a bi-modal grain size distribution in the plastic deformation was addressed by Berbenni et al. [21] using the crystal plasticity framework. The latter demonstrated a strong impact of grain size dispersion on strain-hardening capacity and ductility especially with the reduction of the sub-grain size to several microns, while the random grain size is by a factor of 10 to 20 higher, which is relevant grain size distribution for commercial heavily forged tungsten grades. Another important limitation of the model is its incapability to treat the irradiation induced hardening due to the lattice defects which experience modification of their properties as plastic flow progresses (the absorption and transformation of dislocation loops in BCC metals [22] and stacking fault tetrahedral in FCC metals [23] are well known phenomena). Hence, further development of the crystal plasticity model for polycrystalline tungsten is needed to overcome the above mentioned shortcomings.

In this work, we continue the investigation of the strain-hardening behavior by using a recently developed self-consistent thermo-mechanical model [24]. The model was originally developed for FCC copper and was successfully applied to describe not only the temperature effects but also neutron irradiation defects affecting the strain-hardening response. The model therefore can treat both effects of irradiation defects and pre-existing microstructures accounting for the stress-thermal activation proving dislocation-mediated slip. While the thermal activation effects are treated at the grain level by means of a tensorial plasticity crystal model, the elastic–viscoplastic self-consistent approach [25–28] is applied for the scale transition from individual grains to macroscopic polycrystalline. Here, we applied this model to treat the stress–strain behavior of commercial polycrystalline tungsten grades in the as-received (i.e. heavily plastically deformed) and annealed states. A unique parameterization set is designed and found to predict well both yield stress and work-hardening regime in the temperature range 773–1273 K (i.e. 500–1000 °C), as above it the role of creep in the course of standard tensile test is

becoming prominent. The output of the formulated model was validated using the transmission electron microscopy (TEM) examination of the samples deformed at 873 K up to 5%, 20% and 28% strain. A good agreement for the dislocation density was found up to 20% of strain deformation, while at 28% a certain grain refinement was seen to take place, indicating physical limitations of the current model. However, the already developed model is suitable to enable consideration of the effect of neutron irradiation on the yield stress and post-yield work-hardening stage of commercial polycrystalline tungsten, which are the crucial elements in the constitutive laws for the application in the finite element analysis.

## 2. Experimental procedure: mechanical tests and microstructural analysis

The pristine material used in this study was a polycrystalline W of 99.99% purity, provided in a rod form by Plansee AG [29]. The main impurities, as reported by the manufacturer, are listed in Table 1. The removal of initial residual stresses was performed by a thermal treatment at 1273 K, followed by recrystallization at 1873 K for 1 h. A typical grain size of the material was about 50–150  $\mu\text{m}$ .

Two types of samples were produced from the double forged rods, namely: ‘transversal’ and ‘longitudinal’, referring to the orientation of the bars with respect to the second axis of forging. Here, we shall use the results obtained for the ‘longitudinal’ samples. Tensile testing was performed in a high temperature vacuum furnace on samples with an overall length of 26 mm, a gauge length of 15 mm and an effective cross-section of  $3 \times 3 \text{ mm}^2$  [30]. The tests were conducted in air at 500 °C and in vacuum ( $10^{-2}$ – $10^{-3}$  mbar) at 1000 °C, applying the deformation rate of 0.2 mm/min which corresponds to a strain rate of  $2.2 \times 10^{-4} \text{ s}^{-1}$ .

The pristine microstructure of the tungsten was found to play an important role in the deformation behavior [31]. The microstructure of as-received, as-annealed and plastically-deformed samples was studied by transmission electron microscopy (TEM) as well as by electron back scattering diffraction (EBSD) analysis.

For the in-depth microstructural investigation of the effect of plastic deformation, several macro-flat tensile samples were cut by electric discharge machine (EDM) from the middle of the supplied rod, as shown in the drawing given in Fig. 1.

To release the stress introduced by the electric discharge machining, the tensile sample was re-annealed at 1273 K for 1 h in an argon (Ar) atmosphere. Several tensile tests were performed at 873 K in air at a deformation rate of 0.2 mm/min to reach 5%, 10%, 20% and 30% deformation. The latter approximately corresponds to the ultimate tensile strength of the studied grade. TEM and EBSD samples were cut from the middle of the sample and re-annealed at 873 K for three hours prior to the examination.

**Table 1**  
Impurity content of the tungsten batch, as specified by the supplier.

Impurities	Ag	Ba	Co	Fe	Mn	Ni	Ti	Mo	Co	O	Si	Al	Ca	Cr	K
$\mu\text{g/g}$	10	5	10	30	5	5	5	100	30	20	20	15	5	20	10
Impurities	Na	Pb	Zn	H	Pb	As	Cd	Cu	Mg	Nb	Ta	Zr	N	S	
$\mu\text{g/g}$	10	5	5	5	20	5	5	10	5	10	20	5	5	5	

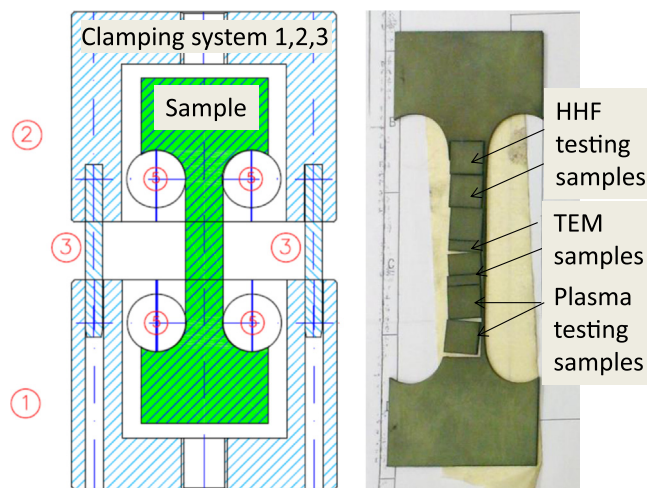


**Fig. 1.** Flat macro-sample for tensile testing. The left-hand side shows the sample geometry and clamping system, while the right-hand side shows a picture of the loaded sample after EDM cutting to produce samples for TEM examination, high heat flux (HHF) testing and plasma interaction testing, used in our previous works.

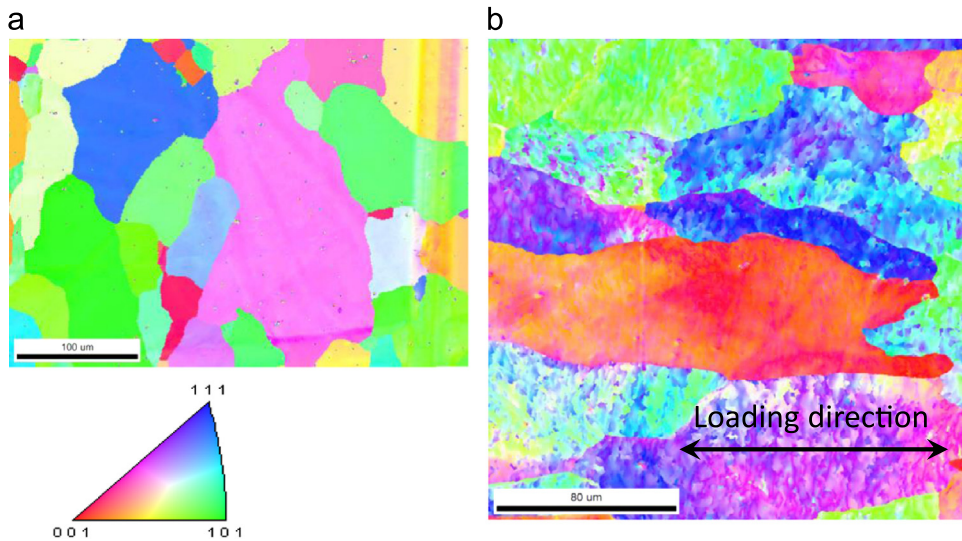


**Fig. 2.** Inverse pole figure maps of tungsten in the (a) as-annealed and (b) as-deformed (28% strain) conditions. The arrow in (b) shows the tensile loading direction. (For interpretation of the references to color in this figure, the reader is referred to the web version of this article.)

Generally, the microstructure of both types of the samples consisted of large random grains (separated by high angle GB interfaces), which contained subgrains (separated by low angle GB interfaces), with dislocations present inside grains as well as at the low angle GB interfaces. Upon thermal annealing, microstructural recovery was expressed in a limited sub-grain growth, removal of a significant amount of subgrains and reduction in dislocation density.

The dislocation density in the as-received tungsten was  $(2 \pm 0.5) \times 10^{13} \text{ m}^{-2}$  and the average grain size was about  $50 \mu\text{m}$  respectively. The average size of the subgrains was  $3\text{--}5 \mu\text{m}$ . The fraction of low angle GBs in the as-received tungsten was around 80–90%, thus the majority of the GB interfaces was of low angle type i.e. dislocation walls [19].

The microstructure of the annealed and then plastically deformed tungsten samples was studied here. SEM analysis of the as-annealed samples revealed the growth of the random grains up to  $150 \mu\text{m}$ , and the strong reduction of the fraction of low angle GBs down to about 20%. The example of the EBSD maps is given in Fig. 2, which shows the inverse pole figure maps for the as-annealed and plastically-deformed samples. Three main crystallographic orientations of the BCC lattice (i.e.  $\langle 111 \rangle$ ,  $\langle 001 \rangle$  and  $\langle 101 \rangle$ ) are indicated on the maps, by a blue, red and green color respectively, to denote the orientation of corresponding grains. From Fig. 2, one can see that large random grains are practically free of subgrains, although rather small grains (of size  $5\text{--}10 \mu\text{m}$ ) are rarely present. This is in strong contrast with the as received material (see figures and detailed description in Ref. [19]), where a frequent color contrast inside large random grains indicated the presence of numerous subgrains. In the case of the deformed material, the effect of tensile loading is obvious and one can see that the grains are elongated in accordance with the orientation of the sample with respect to the tensile loading direction. However, the applied deformation did not result in the visible grain refinement, at least was not clearly detectable by means of EBSD techniques. To provide a deeper insight in the possible microstructural modifications induced by plastic deformation we performed TEM investigation.

The TEM samples ( $10 \times 3 \times 1.25 \text{ mm}^3$ ) were extracted from the middle of as-annealed and as-deformed samples (plates of dimensions with  $10 \times 10 \times 1.25 \text{ mm}^3$ ) by EDM (see Fig. 1). These pieces were then mechanically polished from both sides using SiC paper with grit sizes of 220, 500, 1200 and 4000 to achieve  $70\text{--}100 \mu\text{m}$  thickness and further cut with a wire cutter into pieces to fit  $3 \text{ mm}$  TEM grids. They were polished again from both sides with 4000 SiC paper to remove the remnants of a glue, rinsed in acetone and ethanol and then glued on  $3 \text{ mm}$  copper grids with an aperture of  $1 \text{ mm}$ . Finally, the specimens were polished electrochemically with a solution of 1.5 wt% NaOH in water with applied voltage of 15 V. The specimens were investigated with JEOL 2010 TEM operating at 200 kV and JEOL 3010 TEM operating at 300 kV. The examples of the bright field TEM images of dislocations observed in as received and plastically-deformed samples are presented in Fig. 3. The presence and density of dislocations was seen to be inhomogeneous in the as-received sample even within a single grain. After plastic deformation, the dislocations become evident over the visible area reducing the inhomogeneity of their spatial distribution, but still some places contained clearly large dislocation tangles. The average dislocation density was measured following the method used in [32]. Several calculations at different areas of the specimen are performed to get an average number of dislocation density. Each calculation requires a TEM micrograph, corresponding diffraction pattern and convergent beam electron diffraction (CBED) pattern. In Digital Micrograph software, provided with the image sensor of a microscope, a circle is drawn randomly in an image and the number of intersections of it with dislocation lines is counted. Dislocation density is then calculated as  $\rho = 2N/Lt$ , where  $N$  is the number of intersections of the circle with dislocation lines,  $L$  is the length of the circle,  $t$  is the local thickness of the specimen at the area of the image. The length of the circle is automatically calculated in the Digital Micrograph software. The local thickness of the specimen is



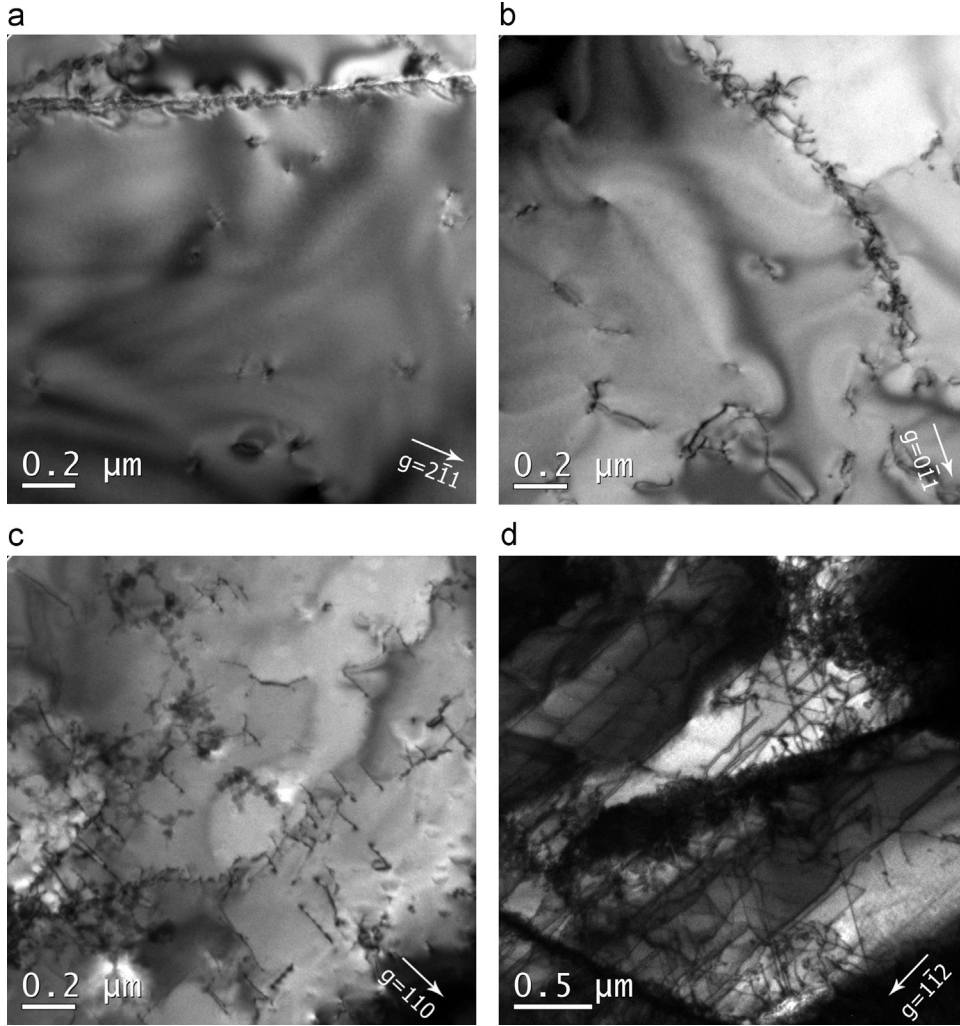


**Fig. 3.** TEM micrographs showing a typical dislocation pattern in tungsten corresponding to (a) as-annealed condition,  $g=(2\bar{1}1)$  and close to a  $[113]$  zone axis; (b) 5% deformed,  $g=(0\bar{1}1)$  and close to a  $[011]$  zone axis; (c) 20% deformed,  $g=(110)$  and close to a  $[001]$  zone axis; (d) 28% deformed, and  $g=(1\bar{1}2)$  and close to a  $[111]$  zone axis.

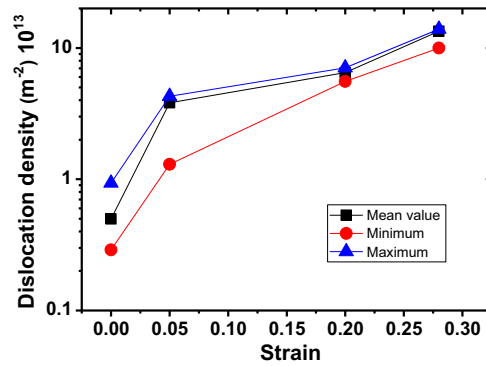


**Fig. 4.** Dislocation density measured in the annealed double forged polycrystalline tungsten by the TEM examination in the as-annealed, and plastically-deformed (at 600 °C) conditions. The indicated 'Minimum' and 'Maximum' curves indicate the limiting values obtained for the dislocation density computed in different regions of the samples (see text noting the inhomogeneous distribution of dislocations).

determined from the CBED pattern and diffraction pattern. The resulting value is given in Fig. 4. In addition to the mean value we have added the upper and lower dislocation density limits, estimated on the basis of all successful TEM images made, to demonstrate the magnitude of the spread from the mean value.

It is to be noted that while only screw straight dislocation segments with Burgers vector  $a_0/2\langle 111 \rangle$  were observed in as-received and 5% deformed samples, a dense tangle dislocation network (with a significant presence of edge component) was found in 20% and 28% deformed samples. Moreover, in the 20% deformed samples, regions with dense dislocation pile-ups forming next to the GB interfaces were regularly seen, and in the 28% deformed sample a limited grain refinement started to take place. The latter can apparently be explained by local sub-grain re-orientation under heavy plastic deformation. Several TEM micrographs demonstrating the above reported observations can be found in the online [Supplementary material](#). The results for dislocation density and above mentioned observations will be taken into account when validating the computational model described below.

Prior we proceed with the computational model, it is important to remind that all TEM investigations were performed ex-situ at room temperature after the deformation at elevated temperature. The TEM samples were extracted from bulk by double side polishing, and therefore we exclude any possible surface effect on the observed dislocation-type microstructure.

### 3. Computational model

Physically, there are two regimes of dislocation-mediated plastic deformation: (i) so called thermal, where the movement of dislocations is thermally activated, hence plastic deformation is controlled by the stress-thermal activation of dislocations and their junctions originating from dislocation–dislocation interaction and (ii) athermal, in which plastic deformation is controlled by microstructural features limiting dislocation movement such as grain or lath boundaries, carbides, etc. High temperature plastic deformation implies the operation of the second regime. Here, we used the data of the tensile tests obtained in the range 500–1000 °C, in which the polycrystalline tungsten is already ductile but the creep contribution is still limited [31]. However, let us start from the construction of the model to treat a single grain in the regime where the plasticity is controlled by the thermally activated movement of screw dislocations.

The currently applied model is based on the recently presented self-consistent approach treating thermo-mechanical properties of FCC single and polycrystals [33]. Here, we adapt this model to treat BCC single- and polycrystalline tungsten. Full details can be found in the original work [24], while here we provide only essentials reflecting the difference in the treatment of FCC and BCC polycrystals (particular to the polycrystalline tungsten).

#### 3.1. Single-grain crystal plasticity model

Following the classical crystal plasticity theory, the gradient of the applied deformation can be decomposed into elastic and plastic contributions [34]. While the elastic part is defined by the elastic moduli and yield point (and their dependence on temperature), the plastic contribution originates from the slip provided by the dislocation movement, which its treatment is at the core of the present model. The viscoplastic strain rate is given by the following expression:

$$\dot{\epsilon}^{vp}(T) = \sum_{\alpha=1}^{N_s} R^{\alpha} \dot{\gamma}^{\alpha}(T) \quad (1)$$

where  $N_s$  is the number of slip systems,  $R^{\alpha}$  is the Schmid factor and  $\dot{\gamma}^{\alpha}(T)$  is the plastic shear rate.  $N_s$  is taken to be 24 following the general practice for modelling of plasticity in BCC metals where  $\langle 111 \rangle \{110\}$  and  $\langle 111 \rangle \{112\}$  are the primary slip systems [35]. The Schmid factor tensor is conventionally defined as  $R^{\alpha} = \frac{1}{2}(s^{\alpha} \otimes n^{\alpha} + n^{\alpha} \otimes s^{\alpha})$ , where  $n^{\alpha}$  and  $s^{\alpha}$  are the unit vectors representing normal to a slip plane and the direction of slip for each particular slip system.

The plastic shear rate in each particular slip system can be defined as [36]

$$\dot{\gamma}^{\alpha}(T) = \dot{\gamma}_0 \left( \frac{\tau_{RSS}^{\alpha}}{\tau_{CRSS}^{\alpha}(T)} \right)^{\frac{1}{m}} \quad (2)$$

here,  $\dot{\gamma}_0$  is the reference shear rate,  $\tau_{RSS}^{\alpha}$  is the current resolved shear stress (RSS),  $\tau_{CRSS}^{\alpha}$  is the critical resolved shear stress (CRSS) needed to initiate the dislocation slip, and  $m$  is the strain rate sensitivity factor.

The resolved shear stress is correspondingly defined by relating the Schmid factor tensor with the Cauchy stress  $\sigma$  as

$$\tau_{RSS}^{\alpha} = R^{\alpha} : \sigma \quad (3)$$

The CRSS in slip system  $\alpha$  was defined as a linear sum of three temperature- and microstructural-dependent components:

$$\tau_{CRSS}^{\alpha}(T) = \tau_f(T) + \tau_{dis}^{\alpha}(T) + \tau_{GB}(T) \quad (4)$$

here,  $\tau_f$  is the lattice friction stress, being is the Peierls stress for a screw dislocation at zero temperature,  $\tau_{dis}^{\alpha}$  is the stress coming from the dislocation–dislocation interaction (so called forest dislocation hardening),  $\tau_{GB}$  is the strengthening originating from the dislocation–GB interaction. The latter term is taken into account when treating polycrystals.

The functional for the lattice friction stress  $\tau_f(T)$  has been adopted from [16]:

$$\tau_f(T) = \tau_{f0} \left( 1 - \frac{k_B T \ln(\dot{\gamma}_{p0}/\dot{\epsilon})}{2H_k} \right)^2 \quad (5)$$

where,  $\tau_{f0}$  is the Peierls stress for the screw dislocation,  $k_B$  is the Boltzmann constant,  $\dot{\gamma}_{p0}$  is the reference strain rate,  $2H_k$  is the formation enthalpy of the kink pair on a screw dislocation, and  $\dot{\epsilon}$  is the applied strain rate.

The effective dislocation forest hardening in each particular slip system,  $\tau_{dis}^\alpha(T)$ , is defined as

$$\tau_{dis}^\alpha(T) = b\mu(T)\sqrt{h_{dis}(T)\rho_{dis}^\alpha(T)} \quad (6)$$

where,  $b$  and  $\mu$  are the magnitudes of the Burgers vector and the shear modulus, respectively.  $h_{dis}$  is the dislocation–dislocation interaction strength and  $\rho_{dis}^\alpha$  is the dislocation density in slip system  $\alpha$ .

Strengthening defined by the GBs, following the Hall–Petch effect formulation, is introduced via the empirical relationship [37]:

$$\tau_{GB}(T) = k_{HP}(T)d^{-0.5} \quad (7)$$

where  $k_{HP}$  is the Hall–Petch strengthening coefficient and  $d$  is the average grain size.

The evolution of dislocation density in each particular slip system,  $\rho_{dis}^\alpha(T)$ , was described following the law proposed by Mecking and Kocks [20]:

$$\dot{\rho}_{dis}^\alpha(T) = \dot{\gamma}^\alpha(T) \left( k_1 \sqrt{\rho_{dis}^\alpha(T)} - k_2^\alpha(\dot{\epsilon}, T) \rho_{dis}^\alpha(T) \right) \quad (8)$$

The evolution of dislocation density is thus defined by the balance of dislocation multiplication (due to the dislocation–dislocation pinning) and recovery/storage occurring via dislocation–dislocation annihilation and dislocation–GB interaction. These two principle processes are effectively parameterized by introducing temperature dependent coefficients:  $k_1$  and  $k_2^\alpha$ . The second coefficient, in a general case, also depends on the orientation of the particular slip system  $\alpha$ . The mutual relationship between these two coefficients is adopted following the work of Beyerlein and Tome [38] as

$$\frac{k_2^\alpha(\dot{\epsilon}, T)}{k_1} = \frac{\chi b}{g^\alpha} \left( 1 - \frac{k_B T}{D^\alpha b^3} \ln \left( \frac{\dot{\epsilon}}{\dot{\epsilon}_0} \right) \right) \quad (9)$$

here  $\chi$ ,  $g^\alpha$ ,  $D^\alpha$ ,  $\dot{\epsilon}_0$  are respectively, the interaction parameter, the normalized activation energy, a proportionality constant and a reference strain rate.

The temperature dependent shear modulus is defined as

$$\mu(T) = \sqrt{C_{44}(T)(C_{11}(T) - C_{12}(T))/2} \quad (10)$$

and the elastic constant  $C_{ij}$  are taken from the experimental work by Lowrie and Gonas [39].

### 3.2. Treatment of a polycrystalline representative volume element

To get the elastic–viscoplastic response of a polycrystalline volume defined by the heterogeneous evolution of numbers of individual grains (constituting that polycrystalline), a representative volume element (RVE) occupying region  $V$  and consisting of  $N$  individual grains is considered [40]. The RVE is subjected to an external strain rate  $\dot{\mathbf{E}}$ . Following [28], the macroscopic strain rate  $\dot{\mathbf{E}}$  and stress rate  $\dot{\mathbf{\Sigma}}$  defined by the contributions of  $N$  grains can be expressed as

$$\dot{\mathbf{E}} = \sum_{i=1}^N f_i \dot{\epsilon}_i \text{ and } \dot{\mathbf{\Sigma}} = \sum_{i=1}^N f_i \dot{\sigma}_i \quad (11)$$

where  $f_i$  is the volume fraction of the  $i$ -th grain in the RVE.  $\dot{\epsilon}_i$  and  $\dot{\sigma}_i$  denote the average rates of strain and stress in the  $i$ -th grain, respectively.

The elastic–viscoplastic constitutive equation for an individual  $i$ -th grain takes the form:

$$\dot{\epsilon}_i = \dot{\epsilon}_i^e + \dot{\epsilon}_i^{vp} = \mathbf{S}_i : \dot{\sigma}_i + \mathbf{M}_i : \dot{\sigma}_i \quad (12)$$

where  $\dot{\epsilon}_i^e$ ,  $\dot{\epsilon}_i^{vp}$ ,  $\mathbf{S}_i$  and  $\mathbf{M}_i$  denote, respectively, the elastic strain rate tensor, the viscoplastic strain rate tensor, the elastic compliance tensor and the secant viscoplastic compliance tensor.

The macroscopic elastic–viscoplastic constitutive equation of the polycrystal can be expressed as

$$\dot{\mathbf{E}} = \dot{\mathbf{E}}^e + \dot{\mathbf{E}}^{vp} = \mathbf{S}^e : \dot{\mathbf{\Sigma}} + \dot{\mathbf{E}}^{vp} \quad (13)$$

where  $\dot{\mathbf{E}}^e$  and  $\dot{\mathbf{E}}^{vp}$  denote the elastic and viscoplastic parts of the macroscopic strain rates, respectively. Note that Eq. (13) cannot be taken as the Maxwell's law due to the long memory effects of heterogeneous materials [28].

In this study, we use the secant self-consistent scheme to bridge the macroscopic behavior of polycrystals to the local grain constitutive laws, defined by Eqs. (1)–(7). Based on the self-consistent theory and its further development with a novel homogenization model, the elastic–viscoplastic behaviors of both polycrystalline steels with different microstructures [41] and heterogeneous materials under complex thermo-mechanical loading conditions [42] can be effectively analyzed. According to the elastic–viscoplastic self-consistent method [28], the local strain-rate response of an individual grain can be determined as

$$\dot{\epsilon}_i = \mathbf{A}_i^{\mathbf{C}^e} : \left[ \left( \dot{\mathbf{E}} - \dot{\mathbf{E}}^{vp} \right) + \mathbf{A}_i^{\mathbf{B}^e} : \dot{\mathbf{E}}^{vp} + \mathbf{S}^E : \mathbf{S}^e : \left( \mathbf{C}_i : \dot{\epsilon}_i^{vp} - \mathbf{C}^e : \mathbf{A}_i^{\mathbf{B}^e} : \dot{\mathbf{E}}^{vp} \right) \right] \quad (14)$$

where  $\mathbf{S}^E$  is the Eshelby tensor,  $\mathbf{C}_i$  denotes the elastic stiffness tensor of the  $i$ -th grain and  $\mathbf{C}^e$  denotes its effective counterpart of the polycrystal.  $\mathbf{S}^e$  denotes the macroscopic effective elastic compliance tensor.  $\dot{\mathbf{E}}^{vp}$  can be related to the viscoplastic strain rate tensor as  $\dot{\mathbf{E}}^{vp} = \sum_{i=1}^N f_i^t \mathbf{B}_i^{\mathbf{C}^e} : \dot{\epsilon}_i^{vp}$ . Here, the superscript “ $t$ ” means the transposition of the concentration tensor  $\mathbf{B}_i^{\mathbf{C}^e}$ , which is expressed as  $\mathbf{B}_i^{\mathbf{C}^e} = \mathbf{C}_i : \mathbf{A}_i^{\mathbf{C}^e} : \mathbf{S}^e$  [28].  $\mathbf{A}_i^{\mathbf{C}^e}$  is the elastic strain concentration tensor which is defined by

$$\mathbf{A}_i^{\mathbf{C}^e} = \left( \mathbf{I}_4 + \mathbf{S}^E : \mathbf{S}^e : (\mathbf{C}_i - \mathbf{C}^e) \right)^{-1}, \text{ with } \mathbf{C}^e = \sum_{i=1}^N \left( f_i \mathbf{C}_i : \mathbf{A}_i^{\mathbf{C}^e} \right) \quad (15)$$

here  $\mathbf{I}_4$  is the fourth-order identity tensor, and  $\mathbf{A}_i^{\mathbf{B}^e}$  is the viscoplastic strain concentration tensor:

$$\mathbf{A}_i^{\mathbf{B}^e} = \left( \mathbf{I}_4 + \mathbf{S}^E : \mathbf{M}^e : (\mathbf{B}_i - \mathbf{B}^e) \right)^{-1}, \text{ with } \mathbf{B}^e = \sum_{i=1}^N \left( f_i \mathbf{B}_i : \mathbf{A}_i^{\mathbf{B}^e} \right) \quad (16)$$

where  $\mathbf{B}_i$  denotes the secant viscoplastic compliance tensor of the  $i$ -th grain, and  $\mathbf{B}^e$  represents the effective viscoplastic compliance tensor of the polycrystal.  $\mathbf{M}^e$  is the macroscopic effective viscoplastic compliance tensor. These two strain-concentration tensors obey the following condition:

$$\sum_{i=1}^N f_i \mathbf{A}_i^{\mathbf{C}^e} = \mathbf{I}_4, \quad \sum_{i=1}^N f_i \mathbf{A}_i^{\mathbf{B}^e} = \mathbf{I}_4 \quad (17)$$

Substituting Eq. (14) into Eq. (12), one obtains the stress rate tensor of the  $i$ -th individual grain, so that:

$$\dot{\sigma}_i = \mathbf{C}_i : \mathbf{A}_i^{\mathbf{C}^e} : \left( \mathbf{S}^e : \dot{\Sigma} + (\mathbf{S}^E - \mathbf{I}_4) : (\dot{\epsilon}_i^{vp} - \mathbf{A}_i^{\mathbf{B}^e} : \dot{\mathbf{E}}^{vp}) \right) \quad (18)$$

This way, one can compute the response of a RVE, representing a polycrystalline material, combined by several hundreds of individual grains to externally applied load. The information for individual grains to be passed as input for the computational tool include the information on grain size (multi-modal size distribution can also be used), initial dislocation density (in each individual grain), dislocation–GB interaction strength (see Eq. (7)), and properties of lattice defects which may obstruct dislocation motion (typically that would be mean size, density and dislocation–defect interaction strength). Lattice defects, induced by thermal ageing or irradiation, may affect dislocation movement by increasing the yield stress, and also be subject to transformation/removal by gliding dislocations, thus representing a complex plastically-driven evolving system. An example of the implementation of the dislocation-driven absorption of radiation defects has been recently demonstrated by the application of the presently applied self-consistent model to the treatment of radiation hardening in copper [24].

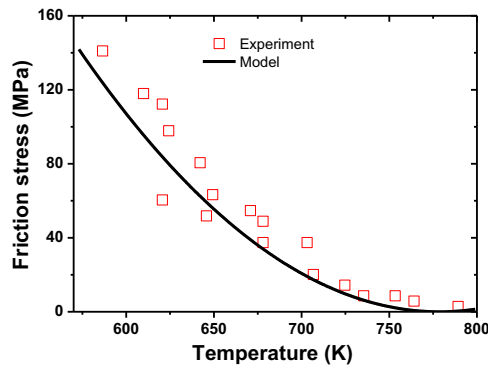


Fig. 5. Lattice friction stress for the dislocation activation according to the model and experimental data from [43].



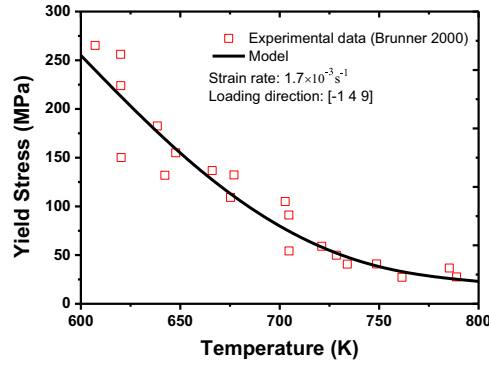


Fig. 6. The temperature dependent yield stress for single crystal tungsten according to the model and experimental data from [44].

## 4. Results and discussion

### 4.1. Application of the crystal plasticity model for a single grain

The critical shear stress for the activation of the dislocation slip as defined in Eq. (5) is drawn in Fig. 5 as a function of temperature and compared to available experimental data taken from [43]. The figure reveals that the assigned enthalpy of 2 eV, attributed to the kink pair formation on a screw dislocation line, agrees well with the experimental data as was previously demonstrated by Lim et al. [16]. Using the established expression for  $\tau_f$  we have assessed the  $h_{dis}$  coefficient in Eq. (6) to fit the yield stress as a function of temperature.

The resulting curve is presented in Fig. 6 and compared to the target experimental data taken from Brunner [44]. The best fit for the  $h_{dis}$  coefficients is given in Table A2 in Appendix A. Applying this parameterization and other input data listed in Table A3 in Appendix A, we have computed the evolution of stress–strain curves for a single crystal W in the temperature range of 600–800 K (i.e. around the experimental ductile to brittle transition temperature) and strain rate of  $1.7 \times 10^{-3} \text{ s}^{-1}$  (typical for standard mechanical tensile tests), taking the initial dislocation density to be  $10^{12} \text{ m}^{-2}$ . The stress–strain curves for the  $[\bar{1}49]$  loading direction are presented in Fig. 7. The corresponding evolution of dislocation density in three different slip systems is given in Fig. 8. The slip systems of  $(\bar{1}01)[111]$  and  $(2\bar{1}1)[11\bar{1}]$  type represent the planes experiencing the highest and lowest resolved shear stress among the active slip systems, given the selected loading direction. Therefore, Fig. 8 demonstrates the upper and lower bounds for the increase of the dislocation density in all active slip systems. Note a negligible increase of the dislocation density in  $(2\bar{1}1)[11\bar{1}]$  slip system due to a very small value of the Schmid factor, displayed on the figure legend.

To demonstrate the impact of loading direction, in Fig. 9 we draw the stress–strain evolution for  $[\bar{1}11]$ ,  $[\bar{1}49]$  and  $[112]$  loading directions, computed at 650 K and strain rate of  $1.7 \times 10^{-3} \text{ s}^{-1}$ . Different Schmid factors impose a variation of the yield stress as a function of applied load. The highest slip resistance of the single crystal realizes in the case of the  $[\bar{1}11]$  load direction.

The evolution of the mean dislocation density (averaged over 24 slip systems) for  $[\bar{1}11]$  and  $[\bar{1}49]$  loading directions is presented in Fig. 10. The latter shows that loading in the  $[\bar{1}11]$  direction results in a faster growth of the dislocation density due to a higher shear stress experienced by the crystal at the moment when the yield point is reached. For both loading directions, the dislocation density is found to grow rapidly up to a strain of 15–20% and then nearly saturates providing an increase by about one order of a magnitude as compared to the initial value.

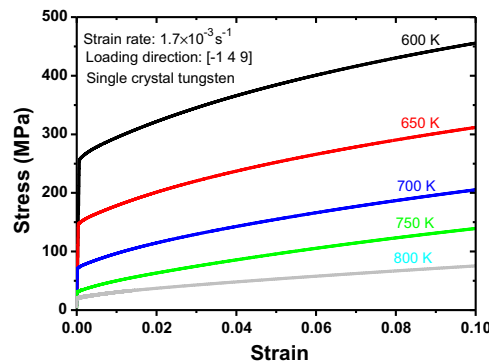
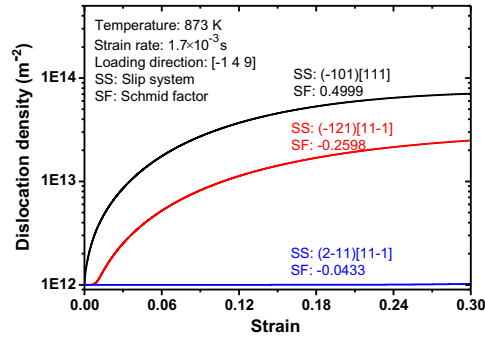
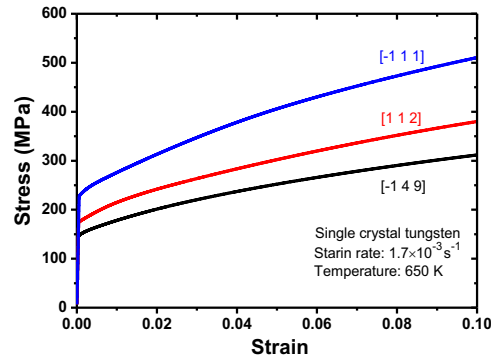


Fig. 7. The stress–strain curves of single crystal tungsten at different temperatures.



**Fig. 8.** The evolution of dislocation density on different slip systems. The initial dislocation density is  $1 \times 10^{12} \text{ m}^{-2}$ . The Schmid factor (SF) is also given in the figure legend for each particular slip plane.



**Fig. 9.** The effect of loading direction on the yield stress and work hardening of a single crystal loaded at 650 K.

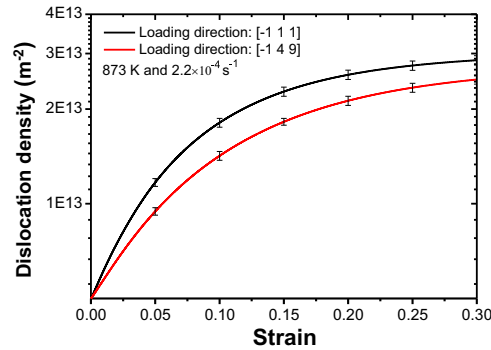


**Fig. 10.** The mean dislocation density (averaged over 24 slip systems) and the standard error for the  $[111]$  and  $[149]$  loading directions.

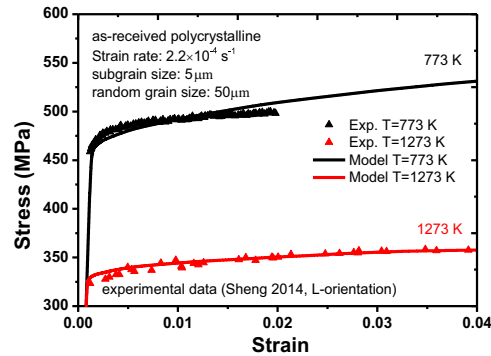


**Fig. 11.** The stress-strain curves of as-received polycrystalline tungsten (samples were loaded in the 'longitudinal' orientation, see details in [19]) at different temperatures. The prediction of the model is shown by full curves.

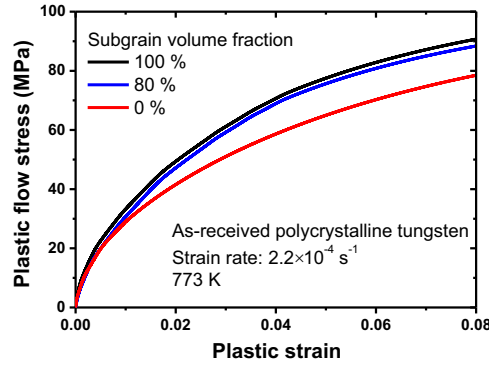
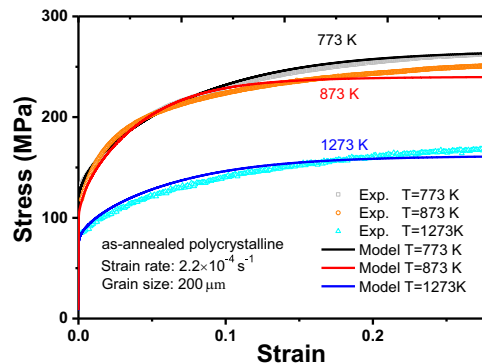


**Fig. 12.** The stress–strain curves corresponding to the plastic deformation in polycrystalline tungsten, calculated using different volume ratio of low- to high angle GBs.

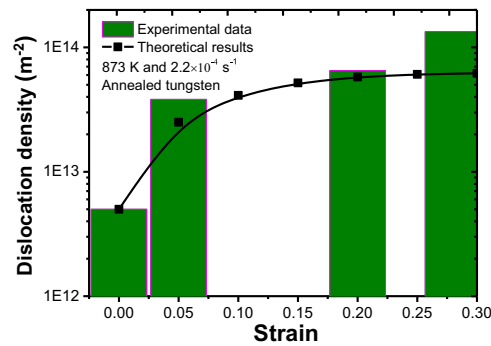
#### 4.2. Application of the self-consistent model for polycrystalline tungsten

Fig. 11 presents a comparison of the results obtained by the above described computational model and experimentally obtained stress–strain curves in the as-received double forged tungsten, which was tested at 773 and 1273 K. The presented results correspond to the tensile testing of a sample by loading in the 'longitudinal' direction (i.e. load is applied along the grain elongation direction, where the elongation originates from the forging). Following the microstructural analysis, we have constructed a model consisting of 400 grains with a bi-modal size distribution aiming to represent large random GBs with a mean size of 50  $\mu\text{m}$  and sub-grains with a mean size of 5  $\mu\text{m}$ . The fraction of sub-grains was taken to be 90%, in line with the experimental EBSD characterization (see section 2). The only adjustable parameter for the model was the Hall–Petch strength coefficient,  $k_{HP}$ , entering Eq. (7). The coefficient was fitted to obtain the best agreement with the experimentally reported yield stress, and was found to be 0.45  $\text{MPa} \sqrt{\text{m}}$  at 773 K, 0.42  $\text{MPa} \sqrt{\text{m}}$  at 873 K and 0.28  $\text{MPa} \sqrt{\text{m}}$  at 1273 K. Interesting to note, these results can be well approximated by a linear dependence as,  $k_{HP} = a - T \cdot b$ , where  $a = 0.72 \text{ MPa} \sqrt{\text{m}}$  and  $b = 3.42 \cdot 10^{-4} \text{ MPa} \cdot \sqrt{\text{m}} \cdot \text{K}^{-1}$ . Such a decrease of Hall–Petch coefficient with the increase of temperature may contribute to the thermally-activated absorption of dislocations by GBs, and followed by the transition of dislocations to neighboring grains or moving along the GB interfaces. Compared with our previous work [19], here we provide the complete set of equation and their parameterization, where thermal activation of plastic deformation and its dependence on dislocation density/grain size is rigorously accounted for. Hence, the present model is general valid to model plastic deformation in tungsten with a variable grain size, dislocation density, deformation rate, deformation temperature, etc.

The experimental uncertainty on the fraction of LAGBs is about 10%, the raw experimental data suggest that the fraction in the as-received material is about 80–90%. To analyse the sensitivity of the model to the choice of the fraction of low- to high angle GBs, we performed calculations fixing the input parameters for the as-received material but varying the fraction of LAGBs from 100% down to 0. The evolution of the flow stress corresponding to the plastic deformation only (i.e. subtracting the yield stress and elastic part of the strain) at 773 K is presented in Fig. 12. The latter reveals that small sub-grains mainly define the work-hardening rate, as expected, and no significant difference in the stress–strain evolution of the crystal composed of sub-grains only or of 80% of sub-grains is present. A considerable reduction in the work-hardening rate is, however, observed for a crystal composed of large random grains. On the basis of these results, we conclude that the particular choice of the fraction of LAGBs in the range of 80–100% is not important for the prediction of the work-hardening behavior in the as-received condition. Note that our model correctly predicts very limited capacity for work-hardening of



**Fig. 13.** The stress–strain curves computed for the as-annealed polycrystalline tungsten at different temperatures. The experimental data are added for comparison.



**Fig. 14.** Dislocation density calculated according to the model in the as-annealed polycrystalline tungsten and experimental data obtained by TEM examination.

the as-received material, which is again related to the fast establishment of high dislocation density in small sub-grains. Hence, the results presented in Figs. 11, 12 and 13 (discussed in the next paragraph) demonstrate that Hall–Petch effect is important not only for the yield stress value but also for the work-hardening rate of the studied here tungsten grades.

Now we move to the application of the model to the as-annealed material. Following the microstructural analysis, the typical grain size is about 50–150  $\mu\text{m}$ . To compute the stress–strain curves for the as-annealed condition, we have taken  $5 \times 10^{12} \text{ m}^{-2}$  as initial dislocation density. The data are plotted along with the experimental results in Fig. 13, which reveals rather good agreement. Note that by increasing the test temperature, the work-hardening capacity decreases, which is explained by the dynamic dislocation recovery and can be correctly captured by the present model.

Our final step is the validation of the applied model, which we realize by comparison of the dislocation density, as predicted by our model and experimentally measured. The TEM observations to get pictures for post-deformation analysis (see Section 2) were performed by selecting the zone axes normal to the slip planes where the maximum resolved shear stress was expected, accounting for the orientation of the inspected grain. Hence, to make an appropriate comparison with the prediction of the model, one should consider the evolution of dislocation density in the slip-systems with a high Schmid factor. For simplicity, we considered all slip systems with the Schmid factor above the mean value, and then computed the average dislocation density. This way, we indeed observe a good agreement with the experimental data, as shown in Fig. 14.

If one considers the mean dislocation density averaged over all 24 slip systems in every grain, its value will be approximately 1/2–1/3 of that presented in Fig. 14. However, we have to note that our experimental investigation also revealed that, focusing on the slip systems with low Schmid factor, the change of dislocation density after deformation is rather low and sometimes even negligible to distinguish. We therefore confirm a general consistency of the experimental results with the prediction of the developed model, at least up to 20% strain.

A considerable deviation, observed for the 28% deformed sample, should apparently be attributed to intensive 3D multiplication of dislocations taking place at late deformation stage, close to the point of the ultimate tensile strength. The formation of concentrated pile-ups and limited grain refinement, observed in the 28% deformed sample (see Section 2 and TEM images in the Supplementary material), are the effects being beyond the physical capability of the present model. Indeed, inclusion of the effects due to a heavy plastic deformation, causing structural changes at the GB level, requires further principle developments in the computation model.

## 5. Summary and conclusive remarks

To summarize, we have performed a combined theoretical and experimental study of the process of plastic deformation, in particular its work-hardening stage, in polycrystalline tungsten. We have utilized a general crystal plasticity framework developed earlier, combined several well-established models to account for dislocation slip, dislocation multiplication and dislocation–GB interaction into a single set of equations, incorporated those within the elastic–viscoplastic self-consistent method, and applied to investigate the plasticity of dedicated polycrystalline tungsten grades. The principal novelty of this work is the direct experimental validation of the evolution of dislocation density at different stages of plastic deformation. We have limited the study in the temperature range of 773–1273 K (i.e. about one third of the melting point), selecting the temperature bounds for a ductile behavior at which the contribution of creep is not yet pronounced (during the tensile test at usual strain rates). The practical need to understand the work-hardening capacity of polycrystalline tungsten comes from its potential application as divertor material in ITER, where cyclic heat load in the considered temperature range (and even beyond it) may cause surface cracking.

The experimental part consists in the mechanical tests and in-depth microstructural characterization including EBSD and TEM analysis performed for both pristine and plastically-deformed material. Thus, the microstructural data served not only as a basis for the parameterization of the model, but also for its validation. The investigated material was the double forged technically pure tungsten, previously engaged in the studies of high heat flux effects [29] and plasma surface interaction

[45]. Both, as-received and as-annealed (at 2073 K) samples were tested. Overall, the annealing was found to remove the majority of sub-grains, and the average size of random grains was seen to increase from 50  $\mu\text{m}$  up to about 100  $\mu\text{m}$ . The dislocation density was also reduced by a factor of two after annealing. The examination of the post-deformed samples revealed that the major impact was on the dislocation density, which grew at least by one order of magnitude, while the size of the random grains nearly did not change, although they become visibly elongated in the samples subject to 28% deformation strain. These data served as a basic microstructural input for the parameterization of the model.

The essence of the self-consistent computational approach, used here, was recently presented by Xiao et al. [24] and applied to study plastic deformation in FCC copper. Here, we make step further and adapt the model for polycrystalline BCC metals accounting for the effect of multiple slip systems, presence of GB limiting dislocation motion. The individual grains, composing a representative volume element, were constructed to respect by-modal size distribution – in accordance with the microstructural examination of the as-received material revealing high fraction of small sub-grains (mainly low angle GBs) contained in large random GBs. The crystal plasticity model, representing the physical core entering the self-consistent integration scheme, was fitted to comply with the experimental data on the yield stress available for a single crystal [12], and also accounting for recent computational analysis performed by Lim et al. [16]. Thus, the single crystal model was defined to account for the role of lattice friction (i.e. activation of dislocation slip) and dislocation–dislocation interaction (i.e. dislocation forest hardening), both being temperature dependent functions. The parameterization set for the dislocation–GB interaction was designed by fitting to our mechanical test data obtained using the polycrystalline tungsten grade. The fitting set included the data only for the as-received samples, and then the model was found to successfully reproduce the stress–strain response of the as-annealed samples by only changing the microstructural input, coming from here performed experimental measurements. Since, the core of the model is based on the dislocation-mediated work-hardening process, the validation against experimental data was performed to ensure the appropriate treatment of dislocation dynamics. Comparison of the experimentally calculated dislocation density with the mean density, computed for the slip planes with a high Schmid factor, revealed a good agreement up to a deformation strain of 20%. Beyond that strain, the formation of dislocation pile-ups and limited grain refinement was observed by TEM, which subsequently defines the range of the applicability of the currently employed model. The latter is probably an issue specific to currently tested tungsten grades with a small size of sub-grains. The latter ensures rather small capacity for work-hardening mediated by dislocation slip and multiplication, and already at 20–25% deformation intensive pile-ups are formed inducing the heterogeneity of dislocation distributions, GB plasticity and probably the formation of microscopic deformation bands. The latter effects are not intended to be captured by the current model.

Nevertheless, we demonstrated that the developed and parameterized model is suitable to accurately predict the stress–strain behavior in a large diapason of plastic strain for polycrystalline tungsten tested in the temperature range of 773–1273 K. Since the present model is a multi-scale physically-based built approach, it has two principle advantages with respect to its perspective application accounting for the plasticity at nano- and micro-meter scales. Firstly, the crystal plasticity model accounts for thermally-activated behavior of plastic slip ensured by dislocations, and therefore can be further upgraded to treat the effect of precipitate- or solute-solution hardening as well as to consider strengthening induced by irradiation defects (and modification of their properties as plastic deformation progresses, as was already demonstrated for FCC copper in [24]). Secondly, the present model allows one to treat multi-modal distribution of grains, hence, enabling to consider polycrystals with complex sub-grain microstructure, and can be adapted further to model the evolution of the grain pattern due to temperature- and stress-induced grain growth or refinement. Subsequently, the present model can serve as a basis for further development to study the degradation of mechanical properties of polycrystalline tungsten under the simultaneous impact of neutron irradiation and heat load – which are being the extreme conditions necessary to be sustained by armor materials in fusion reactors.

## Acknowledgments

This project has received funding from the European Union's Horizon 2020 research and innovation program under Grant agreement no. 633053. The views and opinions expressed herein do not necessarily reflect those of the European Commission. Duan wants to acknowledge the support from the National Natural Science Foundation of China (NSFC) under Grants 11225208. D.T. thanks Prof. Kim Verbeken (UGent) for the assistance in EBSD measurements.

## Appendix A. Parameterization set

The currently developed crystal plasticity model takes into account 24 slip systems of which 12 ones represent dislocation glide in  $\{110\}\langle 111 \rangle$  slip system and 12 in  $\{112\}\langle 111 \rangle$  type. The Hall–Petch coefficient  $k_{HP}$  is fitted to experimental data obtained for the tensile tests at 773, 873 and 1273 K, and found to be 0.45, 0.42 and 0.28  $\text{MPa m}^{0.5}$ , respectively.

See Appendix Table A1–Table A3.



**Table A1**  
Microstructural data for single- and polycrystals.

	Initial dislocation density $\rho_{dis}$ (m <sup>-2</sup> )	Grain size ( $\mu\text{m}$ )	
Single crystal	$1 \times 10^{12\text{a}}$	—	
Polycrystal (as-received)	$2 \times 10^{13\text{b}}$	Subgrains 5 <sup>b</sup>	Grains 50 <sup>b</sup>
Polycrystal (annealed)	$5 \times 10^{12\text{b}}$	200 <sup>c</sup>	

<sup>a</sup> Fitted value, which typically represents dislocation density in the annealed pure BCC metals.

<sup>b</sup> Experimental data from Sheng et al. [46].

<sup>c</sup> The experimental results (see Section 2) show that the grain size varies from 50 to 150  $\mu\text{m}$ , however, 200  $\mu\text{m}$  provides a better agreement with the experiment.

**Table A2**  
Temperature dependent dislocation–dislocation interaction coefficient  $h_{dis}(T)$ .

Temperature (K)	$h_{dis}(T)$
600	0.14
650	0.12
700	0.10
750	0.08
> 800	0.06

**Table A3**  
Parameters for tungsten used in the single crystal model.

Parameter	Definition	Value	Unit	Used in
$N_s$	Number of slip systems	24	Dimensionless	Eq. (1)
$\dot{\gamma}_0$	Reference shear rate	$10^{-3\text{a}}$	s <sup>-1</sup>	Eq. (2)
$m$	Strain rate sensitivity factor	20	Dimensionless	Eq. (2)
$\tau_{f0}$	Friction stress at 0 K	2035 <sup>a</sup>	MPa	Eq. (5)
$k_B$	Boltzmann constant	$1.38 \times 10^{-23}$	J/K	Eq. (5)
$\dot{\gamma}_{p0}$	Reference strain rate	$3.71 \times 10^{10\text{a}}$	s <sup>-1</sup>	Eq. (5)
$H_k$	Double kink activation enthalpy	$1.65 \times 10^{-19\text{a}}$	J	Eq. (5)
$b$	Burger's vector length	2.74	Å	Eq. (6)
$k_1$	Kocks–Mecking parameter	$4.8 \times 10^{8\text{c}}$	m <sup>-1</sup>	Eq. (8)
$\chi$	Interaction parameter	0.9 <sup>b</sup>	Dimensionless	Eq. (9)
$g^{\text{a}}$	Normalized activation energy	$2.8 \times 10^{3\text{c}}$	Dimensionless	Eq. (9)
$D^{\text{a}}$	Proportionality constant	$10^4\text{c}$	MPa	Eq. (9)
$\dot{\epsilon}_0$	Reference strain rate	$10^7\text{b}$	s <sup>-1</sup>	Eq. (9)

For the results obtained in the macro-sample, the value  $k_1 = 9 \times 10^8 \text{ m}^{-1}$ , due to inhomogeneity of the middle part of the bar as compared to the edge part (most densified).

<sup>a</sup> Lim et al. (2015) [16].

<sup>b</sup> Beyerlein and Tome (2008) [38].

<sup>c</sup> Fitted values.

## Appendix B. Supplementary material

Supplementary data associated with this article can be found in the online version at <http://dx.doi.org/10.1016/j.jmps.2015.08.015>.

## References

- Vogler, T.J., Clayton, J.D., 2008. Heterogeneous deformation and spall of an extruded tungsten alloy: plate impact experiments and crystal plasticity modeling. *J. Mech. Phys. Solids* 56, 297–335.
- Roberts, A.P., Garboczi, E.J., 1999. Elastic properties of a tungsten–silver composite by reconstruction and computation. *J. Mech. Phys. Solids* 47, 2029–2055.
- Blomerus, P.M., Hills, D.A., Kelly, P.A., 1999. The distributed dislocation method applied to the analysis of elastoplastic strain concentrations. *J. Mech. Phys. Solids* 47, 1007–1026.

- Clayton, J.D., 2005. Dynamic plasticity and fracture in high density polycrystals: constitutive modeling and numerical simulation. *J. Mech. Phys. Solids* 53, 261–301.
- McVeigh, C., Liu, W.K., 2009. Multiresolution modeling of ductile reinforced brittle composites. *J. Mech. Phys. Solids* 57, 244–267.
- McVeigh, C., Liu, W.K., 2010. Multiresolution continuum modeling of micro-void assisted dynamic adiabatic shear band propagation. *J. Mech. Phys. Solids* 58, 187–205.
- Zinkle, S.J., Busby, J.T., 2009. Structural materials for fission & fusion energy. *Mater. Today* 12, 12–19.
- Zinkle, S.J., 2005. Fusion materials science: Overview of challenges and recent progress. *Phys. Plasmas* 12, 058101.
- Matsuda, S., Tobita, K., 2013. Evolution of the ITER program and prospect for the next-step fusion DEMO reactors: status of the fusion energy R&D as ultimate source of energy. *J. Nucl. Sci. Technol.* 50, 321–345.
- Rieth, M., Armstrong, D., Dafferner, B., Heger, S., Hoffmann, A., Hofmann, M.-D., Jäntschi, U., 2010. Tungsten as a structural divertor material. *Adv. Sci. Technol.* 73, 11–21.
- Giannattasio, A., Yao, Z., Tarleton, E., Roberts, S.G., 2010. Brittle–ductile transitions in polycrystalline tungsten. *Philos. Mag.* 90, 3947–3959.
- Brunner, D., Glebovsky, V., 2000. Analysis of flow-stress measurements of high-purity tungsten single crystals. *Mater. Lett.* 44, 144–152.
- Brunner, D., Glebovsky, V., 2000. The plastic properties of high-purity W single crystals. *Mater. Lett.* 42, 290–296.
- Brunner, D., 2004. Peculiarities of work hardening of high-purity tungsten single crystals below 800 K. *Mater. Sci. Eng. A* 387, 167–170.
- Lennon, A.M., Ramesh, K.T., 2000. The thermoviscoplastic response of polycrystalline tungsten in compression. *Mater. Sci. Eng. A—Struct. Mater. Prop. Microstruct. Process.* 276, 9–21.
- Lim, H.J., Battaile, C.C., Carroll, J.D., Boyce, B.L., Weinberger, C.R., 2015. A physically based model of temperature and strain rate dependent yield in BCC metals: implementation into crystal plasticity. *J. Mech. Phys. Solids* 74, 80–96.
- Pintsuk, G., 2012. Tungsten as plasma facing material. *Compr. Nucl. Mater.* 4, 551–581.
- Zinkle, S.J., 2005. Advanced materials for fusion technology. *Fusion Eng. Des.* 74, 31–40.
- Sheng, H., Van Oost, G., Zhurkin, E., Terentyev, D., Dubinko, V.I., Uytendhouwen, I., Vleugels, J., 2014. High temperature strain hardening behavior in double forged and potassium doped tungsten. *J. Nucl. Mater.* 444, 214–219.
- Mecking, H., Kocks, U.F., 1981. Kinetics of flow and strain-hardening. *Acta Metall.* 29, 1865–1875.
- Berbenni, S., Favier, V., Berveiller, M., 2007. Impact of the grain size distribution on the yield stress of heterogeneous materials. *Int. J. Plast.* 23, 114–142.
- Gelles, D., Schaeublin, R., 2001. Post-irradiation deformation in a Fe–9%Cr alloy. *Mater. Sci. Eng. A—Struct. Mater. Prop. Microstruct. Process.* 309–310, 82–86.
- Robach, J., Robertson, I., Lee, H., Wirth, B., 2006. Dynamic observations and atomistic simulations of dislocation-defect interactions in rapidly quenched copper and gold. *Acta Mater.* 54, 1679–1690.
- Xiao, X.Z., Song, D.K., Xue, J.M., Chu, H.J., Duan, H.L., 2015. A size-dependent tensorial plasticity model for FCC single crystal with irradiation. *Int. J. Plast.* 65, 152–167.
- Capolungo, L., Benkassem, S., Cherkaoui, M., Qu, J., 2008. Self-consistent scale transition with imperfect interfaces: application to nanocrystalline materials. *Acta Mater.* 56, 1546–1554.
- Li, J., Weng, G.J., 2007. A secant-viscosity composite model for the strain-rate sensitivity of nanocrystalline materials. *Int. J. Plast.* 23, 2115–2133.
- Li, J., Weng, G.J., 1997. A secant-viscosity approach to the time-dependent creep of an elastic–viscoplastic composite. *J. Mech. Phys. Solids* 45, 1069–1083.
- Sabar, H., Berveiller, M., Favier, V., Berbenni, S., 2002. A new class of micro-macro models for elastic–viscoplastic heterogeneous materials. *Int. J. Solids Struct.* 39, 3257–3276.
- Uytendhouwen, I., Decreton, M., Hirai, T., Linke, J., Pintsuk, G., Van Oost, G., 2007. Influence of recrystallization on thermal shock resistance of various tungsten grades. *J. Nucl. Mater.* 363–365, 1099–1103.
- Pintsuk, G., Prokhodtseva, A., Uytendhouwen, I., 2011. Thermal shock characterization of tungsten deformed in two orthogonal directions. *J. Nucl. Mater.* 417, 481–486.
- Sheng, H., Uytendhouwen, I., Van Oost, G., Vleugels, J., 2012. Mechanical properties and microstructural characterizations of potassium doped tungsten. *Nucl. Eng. Des.* 246, 198–202.
- Hirsch, P., Howie, A., Nicholson, R., Pashley, D.W., Whelan, M.J., 1977. *Microscopy of Thin Crystals*. Krieger Publishing Company, Malabar, Florida.
- Xiao, X.Z., Song, D.K., Xue, J.M., Chu, H.J., Duan, H.L., 2015. A self-consistent plasticity theory for modeling the thermo-mechanical properties of irradiated FCC metallic polycrystals. *J. Mech. Phys. Solids* 78, 1–16.
- Hill, R., Rice, J.R., 1972. Constitutive analysis of elastic–plastic crystals at arbitrary strain. *J. Mech. Phys. Solids* 20, 401.
- Gröger, R., Bailey, A.G., Vitek, V., 2008. Multiscale modeling of plastic deformation of molybdenum and tungsten: I. Atomistic studies of the core structure and glide of 1/2 {111} screw dislocations at 0 K. *Acta Mater.* 56, 5401–5411.
- Peirce, D., Asaro, R.J., Needleman, A., 1982. An analysis of nonuniform and localized deformation in ductile single-crystals. *Acta Metall.* 30, 1087–1119.
- Hall, E.O., 1951. The deformation and ageing of mild steel. *Proc. Phys. Soc. Lond. Sect. B* 64, 747–753.
- Beyerlein, I.J., Tome, C.N., 2008. A dislocation-based constitutive law for pure Zr including temperature effects. *Int. J. Plast.* 24, 867–895.
- Lowrie, R., Gonas, A.M., 1967. Single-crystal elastic properties of tungsten from 24 to 18,800 °C. *J. Appl. Phys.* 38, 11.
- Duan, H.L., Wang, J., Huang, Z.P., Zhong, Y., 2005. Stress fields of a spheroidal inhomogeneity with an interphase in an infinite medium under remote loadings. *Proc. R. Soc. A—Math. Phys. Eng. Sci.* 461, 1055–1080.
- Berbenni, S., Favier, V., Lemoine, X., Berveiller, A.B., 2004. Micromechanical modeling of the elastic–viscoplastic behavior of polycrystalline steels having different microstructures. *Mater. Sci. Eng. A—Struct. Mater. Prop. Microstruct. Process.* 372, 128–136.
- Mareau, C., Berbenni, S., 2015. An affine formulation for the self-consistent modeling of elasto-viscoplastic heterogeneous materials based on the translated field method. *Int. J. Plast.* 64, 134–150.
- Brunner, D., Glebovsky, V., 2000. Analysis of flow-stress measurements of high-purity tungsten single crystals. *Mater. Lett.* 44, 144–152.
- Brunner, D., 2000. Comparison of flow-stress measurements on high-purity tungsten single crystals with the kink-pair theory. *Mater. Trans. JIM* 41, 152–160.
- Terentyev, D., De Temmerman, G., Minov, B., Zayachuk, Y., Lambrinou, K., Morgan, T.W., Dubinko, A., Bystrov, K., Van Oost, G., 2015. Synergy of plastic deformation and gas retention in tungsten. *Nucl. Fusion* 55.
- Sheng, H., Sun, Z., Uytendhouwen, I., Van Oost, G., Vleugels, J., 2015. Temperature and deformation effect on the low and high angle grain boundary structure of a double forged pure tungsten. *Int. J. Refract. Met. Hard Mater.* 50, 184–190.